ACS APPLIED MATERIALS & INTERFACES

Research Article

Cite This: ACS Appl. Mater. Interfaces 2019, 11, 3482−3492

www.acsami.org

Design and Fabrication of Heterogeneous, Deformable Substrates for the Mechanically Guided 3D Assembly

Haiwen Luan,[†] Xu Cheng,[‡] Ao Wang,[‡,#] Shiwei Zhao,[†,§] Ke Bai,[‡] Heling Wang,[†] Wenbo Pang,[‡] Zhaoqian Xie,[†] Kan Li,[†] Fan Zhang,[‡] Yeguang Xue,[†] Yonggang Huang,[†,∥] and Yihui Zhang*[,‡]

[†]Departments of Mechanical Engineering, Civil and Environmental Engineering, and Materials Science and Engineering and [∥]Center for Bio-Integrated Electronics, Northwestern University, Evanston, Illinois 60208, United States

[‡]Center for Flexible Electronics Technology; AML, Department of Engineering Mechanics, Tsinghua University, Beijing 100084, P. R. China

[§]School of Aeronautic Science and Engineering, Beihang University, Beijing 100191, P. R. China

Supporting Information

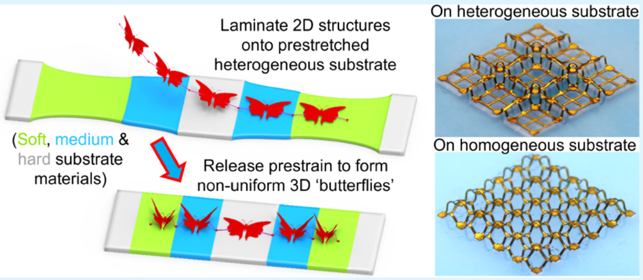

ABSTRACT: Development of schemes to form complex three-dimensional (3D) mesostructures in functional materials is a topic of broad interest, thanks to the ubiquitous applications across a diversity of technologies. Recently established schemes in the mechanically guided 3D assembly allow deterministic transformation of two-dimensional structures into sophisticated 3D architectures by controlled compressive buckling resulted from strain release of prestretched elastomer substrates. Existing studies mostly exploited supporting substrates made of homogeneous elastomeric material with uniform thickness, which produces relatively uniform strain field to drive the 3D assembly, thus posing limitations to the geometric diversity of resultant 3D mesostructures. To offer nonuniform strains with desired spatial distributions in the 3D assembly, this paper introduces a versatile set of concepts in the design of engineered substrates with heterogeneous integration of materials of different moduli. Such heterogeneous, deformable substrates can achieve large strain gradients and efficient strain isolation/magnification, which are difficult to realize using the previously reported strategies. Theoretical and experimental studies on the underlying mechanics offer a viable route to the design of heterogeneous, deformable substrates to yield favorable strain fields. A broad collection of 3D mesostructures and associated heterogeneous substrates is fabricated and demonstrated, including examples that resemble windmills, scorpions, and manta rays and those that have application potentials in tunable inductors and vibrational microsystems.

KEYWORDS: *strain engineering, heterogeneous materials, three-dimensional assembly, buckling, soft materials*

1. INTRODUCTION

Complex mesoscale three-dimensional (3D) architectures have been attracting increasing attention by virtue of their advantageous properties and promising application opportunities in microelectromechanical devices,[1−5] electronics and photonics,[6−11] biomedical sensors,[12,13] metamaterials,[14−21] energy storage systems,[22−25] and so forth. Available fabrication approaches toward 3D mesostructures include additive manufacturing,[24,26−31] two-photon or multiphoton lithography,[32−34] residual stress-induced rolling,[31,35,36] templated growth,[37,38] self-actuation,[39−43] mechanically guided assembly,[31,44−50] and so forth. Although these approaches each possess some compelling capabilities, none is free from limitations. For example, some are inapplicable to device-grade inorganic semiconductors (e.g., monocrystalline silicon), others are incompatible with state-of-the-art planar technologies (e.g., photolithography, thin-film deposition, and laser cutting), and others are inaccessible to complex 3D geometries and/or small characteristic sizes. Among these approaches, the mechanically guided 3D assembly represents a promising approach, as it works seamlessly with nearly all classes of advanced thin-film materials (including semiconductors and metals), over wide-ranging characteristic dimensions (from hundreds of nanometers to tens of centimeters), with remarkable compatibility with modern planar techniques. Persistent research studies have been reported on the development of this assembly approach, for example, to enrich the diversity of realizable 3D geometry by introducing multiple-layer layouts,[45] and origami-/kirigami-inspired designs[46,47] and to strengthen the design tool by developing theoretical models that can serve as the basis of the inverse 3D design.[51,52]

Received: November 1, 2018
Accepted: December 25, 2018
Published: December 25, 2018

DOI: 10.1021/acsami.8b19187
ACS Appl. Mater. Interfaces 2019, 11, 3482−3492

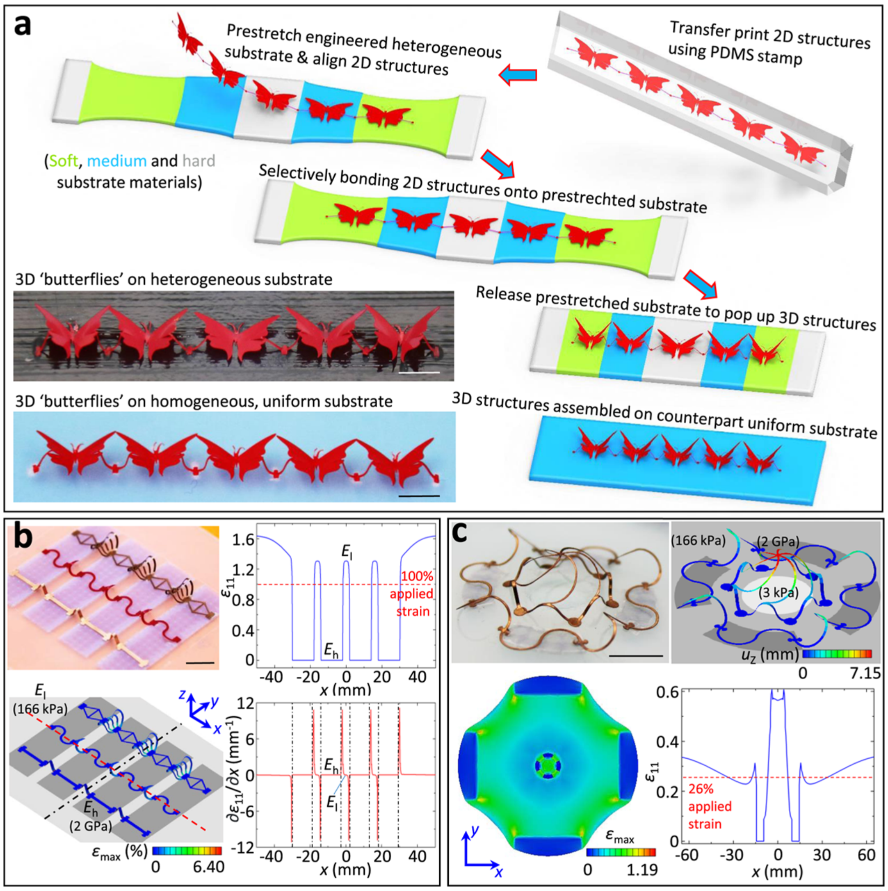

Figure 1. Deterministic 3D assembly through compressive buckling induced by releasing spatially varying prestrain and characteristic resultant 3D mesostructures. (a) FEA results that illustrate the process to assemble 3D "butterflies" based on a heterogeneous, deformable substrate with engineered variation in the material modulus. The engineered heterogeneous substrate is made of elastomers with high (light gray), medium (blue), and low (green) moduli. After releasing the uniaxially prestretched heterogeneous substrate, the 2D precursors are transformed into 3D "butterflies" with spatially varying amplitudes and periodicities, thanks to the spatially nonuniform strain field. As a comparison, the bottom images display the experimental and FEA results for the assembled 3D structure based on a uniform, homogeneous substrate. Detailed fabrication procedures can be found in Experimental Methods and Figures S22 and S24 (Supporting Information). (b) Optical image of the 3D ribbon structures assembled on a heterogeneous substrate with tailored variation of the modulus (top left), relevant FEA results (bottom left), and the distributions of the *x*-direction normal strain and its gradient (bottom right). The overall applied strain (engineering strain) of the substrate is 100%. (c) Optical image of a 3D array architecture, closed-loop circular serpentines and a double-floor hexagonal dome, assembled on a biaxially prestretched heterogeneous substrate (top left), relevant FEA results (top right), a top-view contour of the maximum principal strain in the prestretched substrate (including the clamped regions) (bottom left), and the distribution of the *x*-direction normal strain (bottom right). The overall uniaxial applied strain is 26%. The heterogeneous substrate in (c) features four annulus-sector regions with a modulus of ~2 GPa, a circular region of 3 kPa, and the rest of 166 kPa. The colors of the substrate in (b,c) indicate regions of different moduli, where darker colors denote higher moduli. The colors (except gray) in the FEA results in (b) indicate the magnitude of the maximum principal strain in the 3D structures. The colors (except gray) in the FEA results in (c) indicate the magnitude of the out-of-plane displacement in the 3D structures and the magnitude of the maximum principal strain in the heterogeneous substrates. Scale bars, 5 mm in (a) and 8 mm in (b,c).

Strain engineering of elastomer substrates is promising in controlling the compressive forces applied onto the assembled architectures, rendering a desired spatial distribution for targeted control of the 3D configurations. A variety of complex strain fields can be realized, as demonstrated in recent works on the strain engineering of elastomers.[53−57] Despite the power each method possesses, many of them are not readily applicable to the 3D assembly approach through controlled buckling. The ultraviolet (UV)-based photopatterning approach[54,55] (i) is hard to yield relatively thick substrates (e.g., over 500 μm in thickness) with uniform mechanical properties along the thickness direction because of limitations in light transmittance, (ii) is impotent in achieving designs with a maximum-to-minimum modulus ratio over ~10 from a single kind of substrate material, and (iii) induces the thinning of treated regions. Treating substrate material using Fe^{3+} ion aqueous solution[56] is also difficult to realize heterogeneous substrates with large modulus ratio and/or high resolution in the local control of modulus variation. Stacking patches with higher moduli onto substrates,[57] without proper embedment, fails to produce, on the side of stacking patches, a relatively smooth surface necessary for assembling complex arrays of 3D architectures through mechanical buckling and is not easy to achieve extremely effective strain isolation on the other side. Recently, a scheme of strain engineering devised specifically for the 3D assembly was reported,[53] by tailoring the spatial variation of substrate thickness. Although this approach allows access to many spatially, nonuniform 3D architectures, it is incapable of rendering strain fields with large strain ratios and/or large strain gradients (Figure S1, Supporting Information).

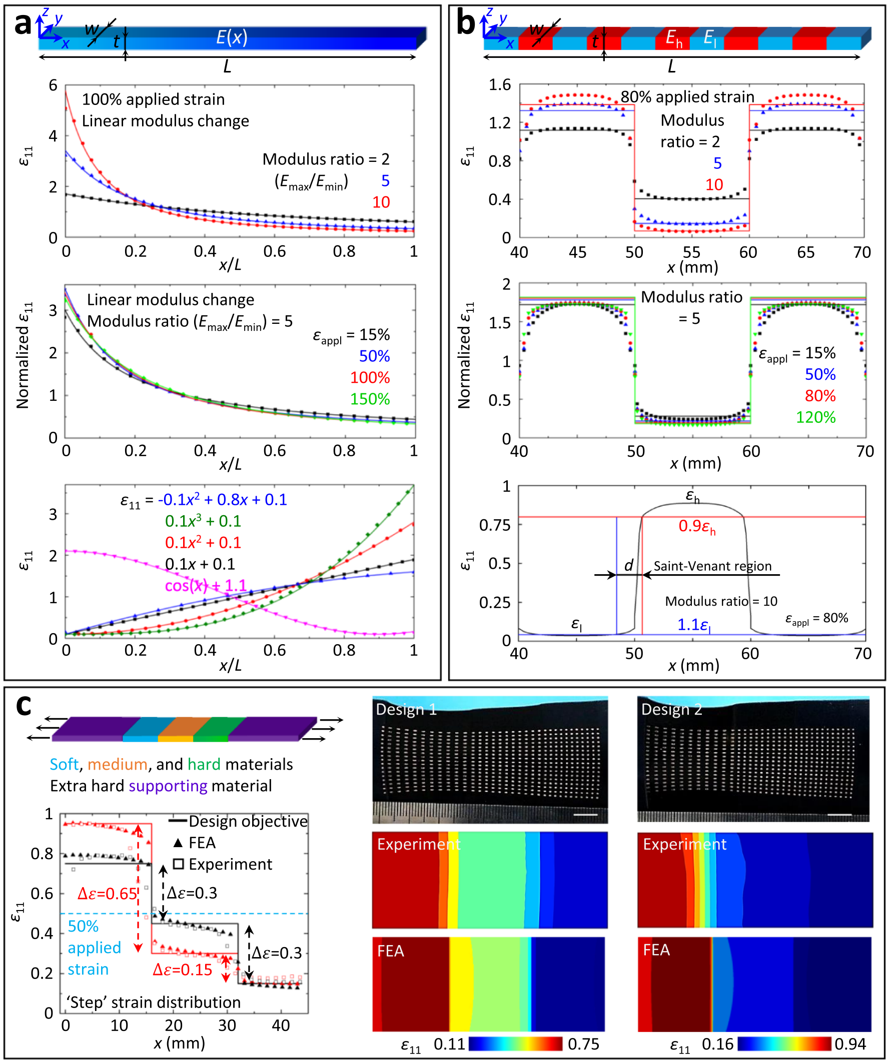

Figure 2. Theoretical and experimental studies on the impacts of different parameters on the strain distributions in uniaxially stretched engineered heterogeneous substrates. (a) Schematic illustration of an engineered heterogeneous substrate with a continuous, unidirectional variation in the elastic modulus $E(x)$ (topmost); the effect of modulus ratios (2, 5, and 10) on the strain distributions in a heterogeneous substrate with a "linear" modulus change for 100% overall applied strain (top); the effect of geometric nonlinearity on the strain profile in a "linear" heterogeneous substrate with a modulus ratio of 5 at four different uniaxial strains (middle); inverse designs to obtain desired strain distributions by tuning the modulus variation profiles of the substrate for 100% overall applied strain (bottom). Lines denote analytical results, and dots denote FEA results. (b) Schematic illustration of an engineered heterogeneous substrate with an alternating, abrupt unidirectional change in the modulus (high modulus E_h vs low modulus E_l) (topmost); the effect of modulus ratios (2, 5, and 10) on the strain distributions in a heterogeneous substrate with an alternating, abrupt modulus change for 80% overall applied strain (top); the effect of geometric nonlinearity on the strain profile in a heterogeneous substrate with a modulus ratio of 5 at four different uniaxial strains (middle); the transition between regions of high and low moduli (defined as the Saint-Venant region) at 80% overall applied strain (bottom). Lines denote analytical results, and dots denote FEA results. (c) Inverse design results for the three-step distributions of strain, enabled by tailored variations in the modulus, as functions of position (left), and the results of optical images, experimental strain visualizations, and FEA strain contours for two inverse designs (middle and right). Designs 1 and 2 correspond to the results marked in black and red, respectively, in the left panel of (c). Scale bars, 8 mm.

Furthermore, the approach of thickness engineering results in a nonflat bottom surface of substrates, which could impose practical issues for testing, observation, or wear comfort when the assembled devices are targeted for applications in wearable electronics. Here, we present a strategy to precisely and effectively engineer the strain profiles of deformable substrates, through the use of substrates with heterogeneous integration of different materials. With proper and effective treatments of interfaces between various substrate materials, engineered heterogeneous, deformable substrates incorporating distinct materials of highly different moduli were manufactured. Sophisticated strain fields with large strain ratios and/or strain gradients can be conveniently realized, according to combined theoretical and experimental studies. On the basis of specially designed heterogeneous, deformable substrates, a large strain magnification (e.g., ~5 times) and an effective strain isolation are also achievable. The precise control of spatially varying prestrain field enables the formation of complex 3D architectures with previously inaccessible geometries. Demonstrations include those that mimic windmills, scorpions, and manta rays and those with potential applications as strain-sensitive 3D inductors.

2. RESULTS AND DISCUSSION

2.1. Conceptual Illustration of the 3D Assembly on Heterogeneous, Deformable Substrates. Figure 1a demonstrates the process for assembly of a 3D architecture consisting of multiple units, each resembling a butterfly, from the corresponding two-dimensional (2D) precursor (Figure S2a, Supporting Information) on a prestretched heterogeneous, deformable substrate. A key distinction from the previous works is the design and fabrication of heterogeneous substrates with spatial variation of the material modulus, in an engineered, controllable manner, enabled by 3D printing and/or casting and curing procedures (see Supporting Information Text 1 for the pros and cons of each procedure). In Figure 1a, the heterogeneous substrate consists of three kinds of elastomeric materials with different moduli, with the soft, medium, and hard materials shown in green, blue, and light gray, respectively. Tensile forces applied to the two ends of the substrate induce spatially varying strain patterns correlated to the strategic variation in the modulus of substrate material. Generally, the tensile stiffness K of the substrate slab [i.e., $K = E(\varepsilon)t(\varepsilon)b(\varepsilon)$, where E, t, and b stand for the elastic modulus of substrate material, thickness, and width, respectively] governs the strain profile. Once the prestretched substrate is released, the spatially varying strain in the substrate then induces the compressive buckling of various degrees at different locations, accordingly forming an array of spatially nonuniform 3D "butterflies" with wings of different tilt angles.

Demonstrated in Figure 1b is an example of uniaxially assembled 3D ribbons (critical width of 400 μm; corresponding 2D precursors shown in Figure S2b, Supporting Information) that extends across interfaces between hard and soft regions (elastic moduli of hard and soft materials are ~2 GPa and 166 kPa, respectively) of a heterogeneous substrate. The ribbons on the left, middle, and right of Figure 1b are made of 30 μm copper foil, 50 μm plastic sheet, and a bilayer of 1 μm copper and 50 μm PET (polyethylene terephthalate), respectively. This design can enable the formation of 3D ribbon architectures consisting of alternatingly flat and buckled shapes, indicating an effective strain isolation, resulted from the extreme modulus ratio ($\sim 10^4$) between the hard and soft regions of the substrate. The simulated results from finite element analysis (FEA, see Supporting Information Text 2 for details) show that under an overall uniaxial stretching strain of 100%, the value of normal strain (ε_{11}) at the surface of the soft region can be up to 128%, while that of the hard region is approximately zero. Moreover, the gradient of x-directional normal strain, $\partial\varepsilon_{11}/\partial x$, can be quite high near the hard–soft interfaces, showing the capability to achieve a rapid strain variation. The 3D geometries predicted by FEA in Figures 1b and S3 (Supporting Information) show excellent agreement with the experimental ones.

The above strategy provides a route to achieve nonuniform strain fields and elaborate 3D mesostructures. Figure 1c demonstrates a collection of 3D closed-loop circular serpentines and a 3D double-floor hexagonal dome (corresponding 2D precursors shown in Figure S2c, Supporting Information), formed on a biaxially prestretched heterogeneous substrate featuring four circumferentially distributed "islands" of the annulus sector with an elastic modulus of ~2 GPa, a circular region of 3 kPa at the center, and the other soft region of 166 kPa. The 3D architecture is made of bilayers of 1 μm copper and 50 μm PET, and the feature size (i.e., the width of ribbon) is 200 μm. The spatially nonuniform strain distribution elaborated in the bottom two panels of Figure 1c contributes to the alternatingly flat and buckled shapes (local prestrain of 60% and zero, respectively) of the outer loop of serpentines and the relatively high degree of compressive buckling (local prestrain of 56%; compared to the applied strain) of the inner dome. Again, FEA predictions show satisfactory agreement with experimental images.

2.2. Theoretical and Experimental Studies of Uniaxially Stretched Heterogeneous Substrates. Figure 2 elucidates how the different design parameters affect the strain distributions in engineered heterogeneous, deformable substrates. An analytical model (see Supporting Information Text 3 and Figure S4, Supporting Information, for details) was developed to calculate the deformations of uniaxially stretched heterogeneous substrates with either continuous or abrupt variation (along the stretching direction) in the elastic modulus $E(x)$.

In Figure 2a (top), a heterogeneous substrate with continuous, unidirectional modulus variation is schematically illustrated, with all sections sharing the same width and thickness before stretching but having different moduli. The maximum modulus ($E_{\max}$) occurs at the right end, where the color is the darkest, and the minimum ($E_{\min}$) at the left end. The modulus ratio ($E_{\max}/E_{\min}$), overall applied strain, and modulus variation profile are the governing parameters of the strain distributions on the top/bottom surface ($z = 0$ for top surface) in substrates with a continuous modulus change. As an example, we take the length, width, and thickness as 40, 10, and 2 mm, respectively. Figure 2a (top) presents the strain distributions in substrates (at 100% applied strain) with the modulus varying linearly but three different modulus ratios. Substrates with a larger modulus ratio tend to render a higher maximum strain at the left end. The ratio of maximum strain to minimum strain, $\varepsilon_{11\text{-max}}/\varepsilon_{11\text{-min}}$, is ~21, 9, and 2.7 for modulus ratios of 10, 5, and 2, respectively. The effect of geometric nonlinearity on the strain profile is shown in Figure 2a (middle) for a heterogeneous substrate with linear modulus change (modulus ratio, 5) under different levels of applied strain. Such nonlinearity is induced by the fact that the soft portion (with low modulus) of the substrate accommodates more and more deformations in comparison to the hard portion (with high modulus), as the stretching proceeds. The profile of modulus variation in the substrate also plays a critical role in defining the strain patterns, which is in direct relevance to the inverse designs targeted for matching precisely the desired strain distributions. Figure 2a (bottom) demonstrates a representative set of strain profiles (at 100% overall applied strain) that are described by five different analytic functions. The equation describing the relation between the target strain distribution and the required substrate modulus distribution is

$$\frac{E(x)}{E(x=0)} = \frac{(\varepsilon_{11}+1)^3}{4(\varepsilon_{11}+1)^4 + (\varepsilon_{11}+1)^3 - 4(\varepsilon_{11}+1) - 1}$$

where ε_{11} is also a function of x. (See Supporting Information Text 3 for details.) Corresponding substrate modulus distributions are shown in Figure S5 (Supporting Information). In all plots in Figure 2a, the analytic results (lines) agree very well with FEA (dots).

Studies on strain distributions in heterogeneous substrates with abrupt, unidirectional modulus variation are presented in Figure 2b. As shown in the schematic, the segments of high

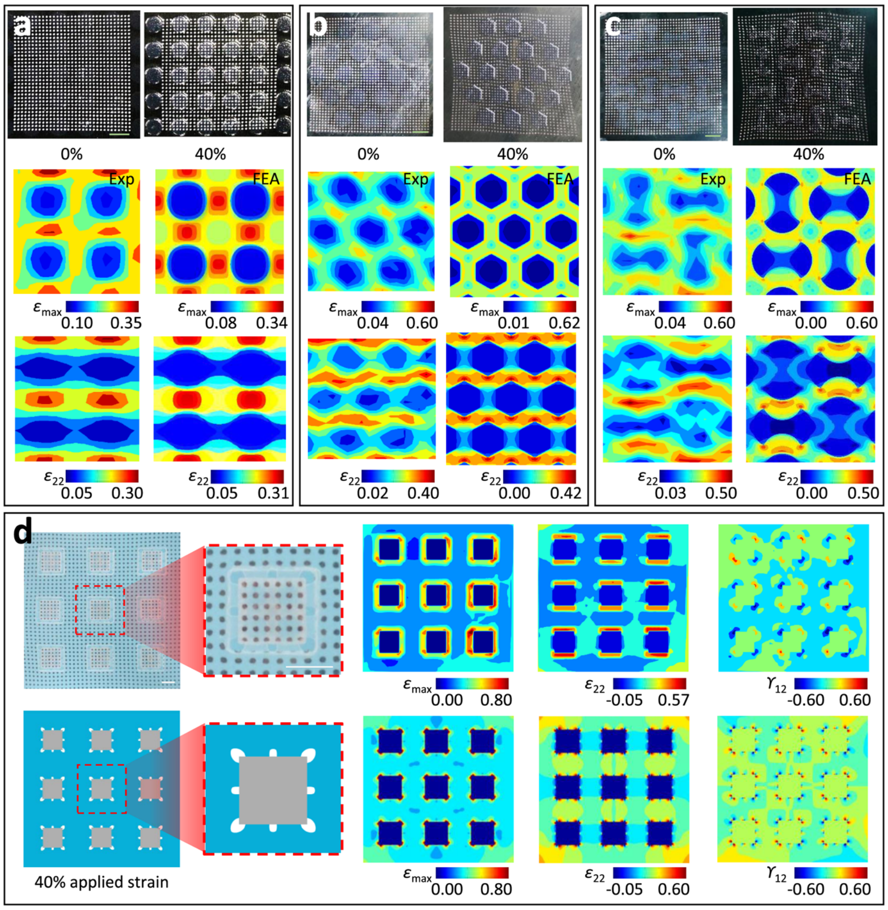

Figure 3. Experimental and theoretical studies on the strain distributions in representative biaxially/multiaxially stretched heterogeneous substrates. (a−c) Optical images of the undeformed and biaxially stretched (40%) configurations (top) and the distributions of strain components (max. principal strain ε_{max} and normal strain ε_{22}) determined from the experiment (middle) and FEA (bottom), for three different heterogeneous substrates [(a) "square" array, (b) "honeycomb" array, and (c) "bone" array]. Arrays of displacement markers are used for strain visualization. Colors in the contour plots denote the magnitude of strain. (d) Optical images (top left) and FEA results (bottom left) of the biaxially stretched (40%) configurations and the distributions of strain components (max. principal strain ε_{max}, normal strain ε_{22}, and shear strain γ_{12}) determined from the experiment and FEA (right) for a heterogeneous substrate with a 3-by-3 array of "islands". Colors in the contour plot denote the magnitude of strain. Scale bars, 8 mm.

modulus (E_h) and low modulus (E_l) are distributed alternatingly in the substrate. Here, the modulus ratio (E_h/E_l) and overall applied strain are critical to the strain distributions on the top/bottom surface ($z = 0$ for the top surface). In our example, the heterogeneous substrate has a total length of 110 mm (10 mm for each segment), a width of 10 mm, and a thickness of 2 mm. Similar to the cases of continuous modulus variation, a higher strain level occurs when a larger modulus ratio is adopted, as shown in Figure 2b (top). The ratio of maximum strain to minimum strain, $\varepsilon_{11\text{-max}}/\varepsilon_{11\text{-min}}$, is ∼23, 10, and 2.8 for modulus ratios of 10, 5, and 2, respectively, according to FEA. The geometric nonlinearity is not conspicuous, as evidenced by the similar curves of normalized strain distributions for four different applied strains in Figure 2b (middle). In Figure 2b (top and middle), analytical results (lines) agree reasonably well with FEA (dots), with the largest deviation less than 10%. The difference results from the fact that the analytical model does not take into account the detailed transition of normal strain between regions of high and low moduli (i.e., the Saint-Venant region). In this study, the Saint-Venant region is defined as the local, transitional portion of the substrate across the hard−soft interface, where the strain level is more than 10% larger than the steady strain level in the low-modulus region and more than 10% lower than that in the high-modulus portion, as displayed in Figure 2b (bottom, for 80% overall applied strain). Detailed studies on the Saint-Venant region, which are essential to understand the deformation behavior near the hard−soft interface, are depicted in Figure S6 (Supporting Information).

The capabilities of analytical and numerical modeling demonstrated here allow strategic engineering of modulus variation to offer desired strain distributions, with either continuous (as demonstrated in Figure 2a, bottom) or abrupt change, at certain strains. Figure 2c provides representative inverse designs (Figure 2c, left, and Figure S7, Supporting Information), which achieve two different triple-step-shaped strain profiles at 50% stretching. Guided by analytical modeling, an initial set of trial modulus distributions was obtained according to the design objectives. Then, elastomer materials (TangoBlack+, FLX9850, and FLX9860, left to right, for Design 1; TangoBlack+, FLX9840, and FLX9860, left to right, for Design 2) available in a commercial 3D printer were selected to match closely the modeling results, although a precise match is very challenging. Experimental strain visualization and FEA were conducted for validating the

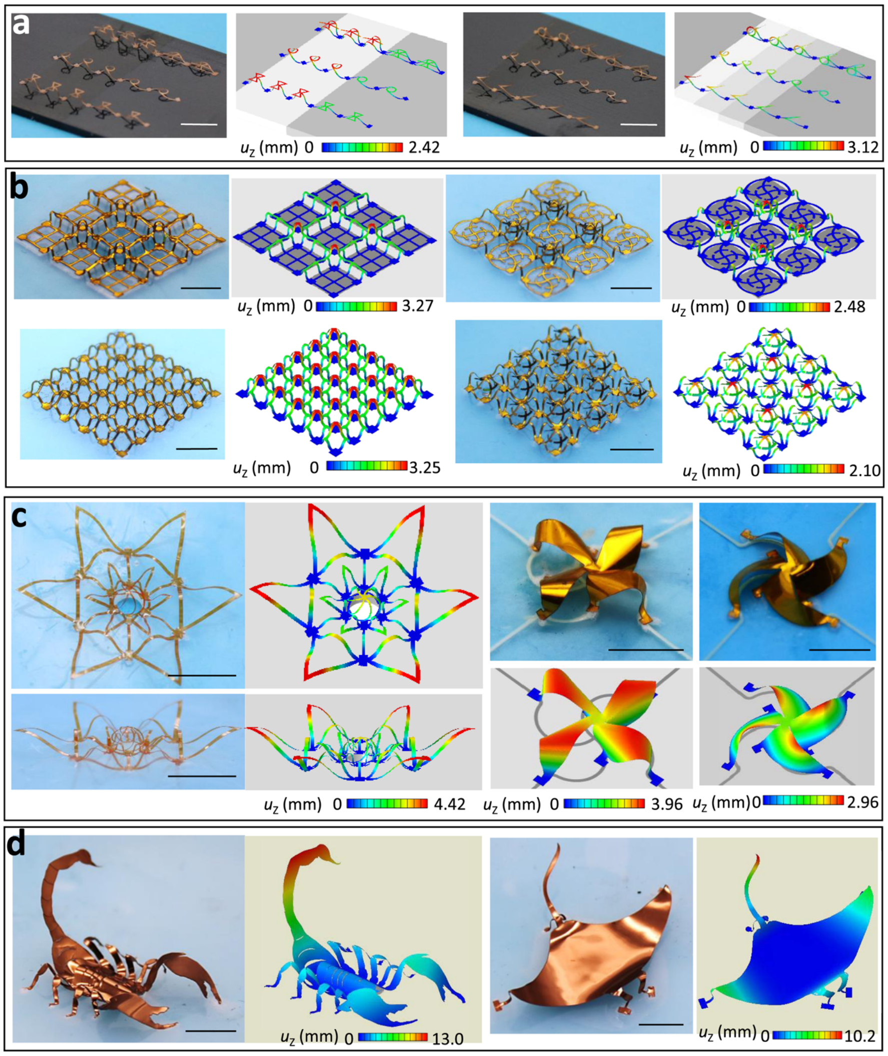

Figure 4. Experimental and computational studies of assorted 3D structures assembled by spatially nonuniform compressive buckling on heterogeneous substrates. (a) Arrays of 3D structures with a unidirectional variation in pivotal geometric characteristics (with periodicities and amplitudes varying distinctly or gradually), together with the corresponding heterogeneous substrates. (b) Arrays of 3D architectures with abrupt changes in geometric attributes, with illustrations of the 3-by-3 "island" substrate. The portions of 3D architectures on the high-modulus substrate regions ("islands") remain flat while the remaining portions pop up. The 3D structures assembled from the same 2D precursors but on uniform, heterogeneous substrates are shown on the bottom for comparison. (c) Radially distributed, interconnected double-ring 3D "flower" assembled on a substrate with a circular hole at the center (left) and two different 3D "windmills" by exploiting different chiralities of the heterogeneous substrates with wavy reinforcement networks while choosing the same 2D precursor (right). (d) A 3D "scorpion" with a raised stinger and a 3D "manta ray" with waving pectoral fins, which are both formed on heterogeneous substrates. Details of the heterogeneous substrates and the relative location of 3D structures on substrates are shown in Figure S19 (Supporting Information). Colors (except gray) in the FEA results indicate the magnitude of out-of-plane displacement for all cases. The substrate colors in the FEA results of (b,c) denote regions of different moduli, and darker colors represent higher moduli. Scale bars, 8 mm.

effectiveness of the inverse design in achieving target strain distributions. Arrays of copper dots (thickness 100 nm, diameter of each dot 600 μm, spacing 1500 μm) generated using sputter deposition served as the markers of strain measurement (see Experimental Methods for details). As shown in Figure 2c (left), the experimental results agree well with FEA, with both matching the targeted strain profiles. Contours of normal strain ε_{11} from both the experiment and FEA are shown in the middle and right panels in Figure 2c for these two inverse designs. The contours of other strain components are presented in Figure S8 (Supporting Information).

2.3. Experimental and Theoretical Studies of Biaxially/Multiaxially Stretched Heterogeneous Substrates.

The above strain-tuning techniques can be extended to biaxial/multiaxial stretched configurations to achieve more sophisticated strain patterns. Here, diverse periodical patterns of high- and low-modulus regions can be exploited in heterogeneous, deformable substrates, with illustrative designs demonstrated in Figure S9 (Supporting Information). Figures 3a and S10 (Supporting Information) demonstrate heterogeneous substrates with "square", "honeycomb", and "bone" features of allocated elastomer materials of higher moduli. When these heterogeneous substrates are subjected to 40% biaxial stretching, the regions with higher moduli deform much less than other regions. Because the elastomeric materials are generally incompressible, the regions with higher modulus become thicker than other regions upon stretching, and therefore, the reflections on the edges are observable in the optical images of the stretched configurations in Figure 3a−c (top). Quantitative measurements of strain fields (using arrays of copper dots as displacement markers, thickness 100 nm, diameter of each dot 450 μm, and spacing 1000 μm; see Experimental Methods for details) in the three different heterogeneous substrates serve to validate the FEA predictions. Upon stretching, the low-modulus regions generally accommodate higher levels of stretching deformations, which could provide more compression for the 3D assembly during the release of prestrain. As demonstrated by various geometric features (e.g., square, triangular, elliptical, and honeycomb patterns) and further combinations, the engineered heterogeneous substrates can provide a diverse range of strain patterns for more sophisticated assembly of 3D structures.

Delicate interface treatment is needed to keep the integrity of the heterogeneous, deformable substrates consisting of materials with drastically different moduli (e.g., modulus ratio $\approx 10^4$ for the following example). As shown in Figures 3d and S10d (Supporting Information), the nine identical "islands" feature interconnected "tunnels" to reinforce their integration with soft matrix materials, such that the entire substrate can be stretched up to 100% without rupture. The "islands" were made of material with high modulus (VeroBlue RGD840, Stratasys, Ltd., ~2 GPa) via 3D printing, whereas the matrix was of soft elastomeric material (Dragon Skin 10 Slow, Smooth-On, Inc., with an elastic modulus of 166 kPa). Without carefully arranged structural details (i.e., interconnected "tunnels" within "islands"), interfacial fractures usually occur before reaching ~30% stretching strain, leading to the full separation of the components with high and low moduli (see Figure S11, Supporting Information, for testing details). By designing the interconnected "tunnels" within "islands", the soft elastomer (Dragon Skin 10 Slow) fills up gaps and forms an interconnected network, ensuring the substrate integrity during stretching and releasing. In the biaxially stretched configurations (from both the experiment and FEA), the substrate remains fully functional, even with observable gaps (see Figures 3d and S12, Supporting Information, for the deformation state of the heterogeneous substrate).

For all these cases in Figure 3, the strain contours based on the experimental measurement and FEA computations match well with each other, thereby illustrating the utility of FEA as a reliable design tool. It is noteworthy that the resolution of visual images of strain fields highly depends on the density of displacement markers. As demonstrated in Figure S13 (Supporting Information), the strain contours determined from a relatively dense array of displacement markers (diameter 0.2 mm for each dot marker, spacing 500 μm) agree better with the FEA predictions of the strain distribution. Additional studies of engineered heterogeneous substrates are shown in Figures S14 and S15 (Supporting Information).

2.4. 3D Structures Enabled by Spatially Nonuniform Compressive Buckling on Heterogeneous Substrates.

The utility of heterogeneous, deformable substrates enables the formation of mechanically assembled 3D structures, either with gradual or dramatic geometrical changes, as illustrated by examples in Figure 4. The 2D precursors can be conformably laminated and selectively bonded onto the uneven surface of the heterogeneous substrate, similar to the cases with uniform, homogeneous substrates. Figure 4a shows a series of spatially changing, unidirectional ribbon structures in bilayers of 1 μm copper and 50 μm PET, with a ribbon width of ~300 μm. The substrate in the left frame of Figure 4a is composed of two different elastomeric materials (TangoBlack+ in the middle and FLX9870 on two sides), whereas the one in the right frame features four different materials (from left to right, FLX9870, TangoBlack+, FLX9850, FLX9860, and FLX9870). Both substrates are designed to produce step-shaped strain profiles. The corresponding strain distributions for both substrates are displayed in Figure S16a (Supporting Information). The spatial distinction in pivotal geometric characteristics (e.g., periodicities and amplitudes) of 3D ribbon structures is evident in Figure 4a. For comparison, the 3D structures assembled from the same 2D precursors (Figure S17a, Supporting Information), on uniform, homogeneous substrates, are displayed in Figure S16b (Supporting Information).

Elaborate 3D arrays of ribbon structures (bilayers of 25 μm polyimide and 200 nm copper) with alternatingly buckled and flat shapes are assembled on the "island" substrates, where "islands" are made of a hard material (VeroBlue), as demonstrated in Figure 4b. The "island" substrate, sharing the same concept with examples in Figures 1b,c and 3d, ensures that the top surface experiences virtually no stretching on the "islands", fulfilling effectual strain isolations in designated regions of the 3D ribbon structures. Therefore, the portions of the 3D architecture on high-modulus regions of the substrate remain flat. The distribution of normal strain ε_{11} along a diameter (in the x-direction) of this kind of substrates is displayed in Figure S15 (Supporting Information). An array of orthogonal straight ribbons is transformed into an interconnected architecture that features flat, single-floor, and double-floor shapes, forming a "plaza" (Figure 4b, top left). Figure 4b (top right) provides another example, in the form of an array of interconnected circular ribbons, which looks like a "garden" after 3D assembly. The assembled 3D structures with the use of the same 2D precursors (Figure S17b, Supporting Information) on uniform, homogeneous substrates are presented in Figure 4b (bottom), to serve for comparison.

In the heterogeneous, deformable substrate designs where part of the substrate has an extremely low (or even zero, i.e., completely void) modulus, the stretched substrate shows highly localized deformations in the ultrasoft portions, providing a viable approach to the application of extremely high prestrains for the 3D assembly. Examples in Figure S14 (bottom, Supporting Information) demonstrate the concept in a 3-by-3 "pond" array heterogeneous substrate. An example of direct relevance to the 3D assembly (Figure 4c, left) involves a through hole at the center of a silicone (Dragon Skin 10 Slow, 166 kPa) substrate. At a biaxially stretching strain of 60%, large radial and circumferential deformations occur around the hole. The equivalent stretching strain, defined as the relative increase in the hole diameter, can be up to ~200%, indicating a strain magnification factor of ~3.3. Experimental results show that the use of an ultrasoft material (Silbione, 3 kPa) has little influence on the substrate deformations, provided that the soft part is ultrasoft enough (3 kPa vs 166 kPa in this case). An interconnected double-ring "flower" is aligned center-to-center on the engineered heterogeneous substrate with a central hole. During the 3D assembly, the inner ring and central dome of the "flower" design undergoes a much larger compression (~200% local prestrain) than the outer ring (~50% local prestrain), forming a fine-layered 3D shape (Figure 4c).

Aside from the relatively regular geometric patterns, sophisticated networks of reinforcement material (with high

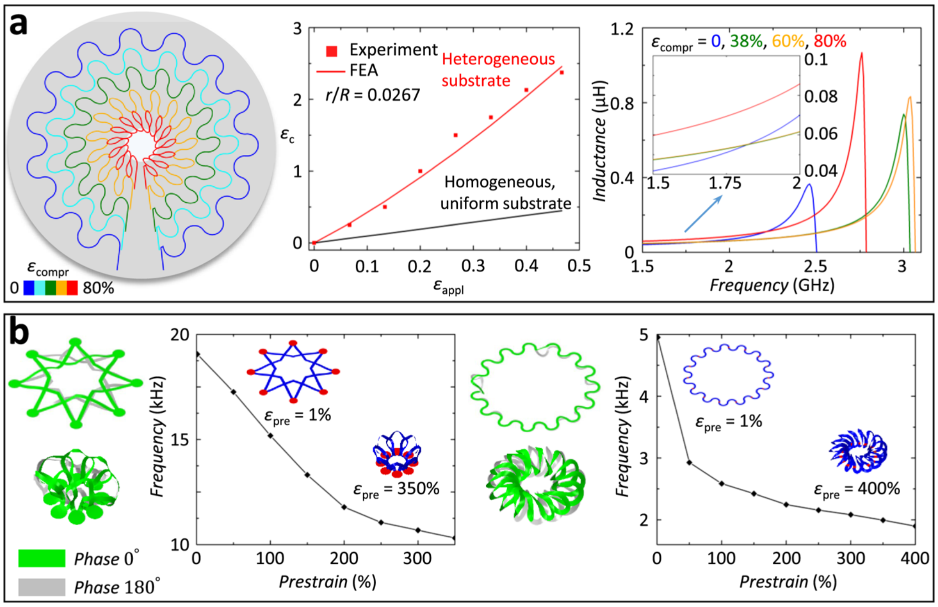

Figure 5. 3D mesostructures with potential applications as tunable inductors and mechano-vibrational devices. (a) 3D toroidal inductor with tunable inductance. A top view of the toroidal coil configurations undergoing compressive strains of 0, 20%, 38%, 60%, 80% with the fully released heterogeneous substrate (only the inner part) featuring an ultrasoft central region shown underneath (left). The toroidal coil (made of copper) has a width of 50 μm, a thickness of 5 μm, and an overall diameter (undeformed) of ∼10 mm. The 3D toroidal inductor is fabricated on the engineered heterogeneous substrate at an overall applied strain of 87%, which produces a localized prestrain of 400% near the central region. The localized stretching strain in the ultrasoft central region of the heterogeneous substrate ($r/R = 0.0267$; the radius of the ultrasoft central region $r = 2$ mm, and half the net spacing between opposite clamps $R = 75$ mm) is shown as a function of the overall applied strain, with the result in a uniform, homogeneous substrate as a comparison (middle). The distinguishable inductance performances for different coil configurations suggest the mechanical tunability (right). (b) 3D structures with tunable resonant frequency formed with ultrahigh prestrain levels (350% and 400% for the structures on the left and right, respectively) on a heterogeneous substrate with an ultrasoft central region. For each structure, the vibration modes for the fully assembled and the slightly popped-up configurations are shown on the left, and the curves of resonant frequency vs prestrain are displayed on the right, showing distinct resonant frequencies for different configurations.

modulus) can be exploited in the design of heterogeneous substrates to convert the external stretching into complex deformations (e.g., those involving rotational motions) in the inner regions of the substrate. Representative designs that illustrate this concept appear in Figure S18 (Supporting Information), where significant localized rotations can be observed through the use of serpentine-shaped reinforcement networks embedded in another soft material. Furthermore, the chirality of the heterogeneous substrates with wavy reinforcement networks can induce different ways of rotation in the 3D assembly, leading to more diverse 3D geometries. Examples of assembled 3D structures on such network-type heterogeneous substrates (Figure S18a, Supporting Information) include two different 3D "windmills" (Figure 4c, right) formed with the same 2D precursor on two heterogeneous substrates chiral to each other.

In addition to the "flowers" and "windmills", other examples of 3D structures that resemble real-world objects include a 3D "scorpion" with a raised stinger and a 3D "manta ray" with waving pectoral fins (Figure 4d). The mechanics of corresponding heterogeneous substrates and locations of 3D structures on substrates are illustrated in Figure S19 (Supporting Information). The 3D "scorpion" has a laterally assembled body and fully popped-up claws and legs. The underlying heterogeneous substrate has a pair of "kidney"-shaped hard parts (made of VeroBlue) located under the body of the "scorpion", providing proper lateral compression for the body while remaining almost undeformed longitudinally. The tail of the "scorpion" is elevated with the aid of a tiny bonding site near the abdomen of the "scorpion", controlling the buckling mode of the essentially bistable "tail". The 3D "swimming manta ray" shows a pair of waving pectoral fins and a smooth, flattened body, thanks to a triangular hard part (VeroBlue), aligned underneath the body of the "manta ray", in the heterogeneous substrate, effectively lowering the prestrain level only at the center.

Additional examples of assembled 3D structures, including a double-loop 3D toroidal array with alternatingly buckled and flat segments and a hybrid 3D membrane-ribbon array with popped-up membranes and flat ribbons, appear in Figures S20 (Supporting Information). The diverse range of accessible 3D geometries demonstrates the capability of the deterministic 3D assembly approach based on engineered heterogeneous substrates.

2.5. Application Implications of 3D Structures Assembled on Heterogeneous Substrates. Assorted 3D structures accessible by this strategy have potential applications in tunable inductors and mechano-vibrational devices. Figure 5a demonstrates a highly compact 3D toroidal inductor (copper, 5 μm thickness) that offers a mechanically tunable inductance. The toroidal coil configurations (from top view) undergoing different compressive strains (ε_{compr} = 0, 20%, 38%, 60%, and 80%) are shown in Figure 5a (left), along with the fully released heterogeneous, deformable substrate (with only the central portion shown). The substrate involved here has an ultrasoft circular region (Silbione, diameter 4 mm) at the center and a relatively hard surrounding region (Dragon Skin 10 Slow, net spacing between opposite clamps 150 mm) to enable an ultralarge localized effective prestrain (400% local prestrain for an overall radial stretching strain of 87%). The strain magnification factor is ∼4.6 for 87% applied strain and ∼5.1 for 47% applied strain, which is difficult to achieve using currently available approaches. The deformation analyses of this kind of heterogeneous substrates are depicted in Figure S21 (Supporting Information). Specifically, Figure 5a (middle) displays the dependence of the localized stretching strain in the central region of the heterogeneous substrate on the overall applied strain, showing a much larger slope than that of the homogeneous substrate. The ultrahigh prestrain level locally rendered following the approach is of a potential value to the design of mechanically tunable microdevices. The inductance performance of different inductor configurations is studied through electromagnetic simulation (Ansys HFSS, see Supporting Information Text 4 for details) and found to differ significantly over varying configurations (Figure 5a, right). The inductance of the 3D inductor at the steady stage (1.5 GHz), which represents an important quantity in practical applications, shows an increase of ∼40% at $\varepsilon_{\mathrm{compr}} = 80\%$, in comparison to that of the 2D inductor. The shift of resonant frequency is related to parasitic capacitance in the inductor-substrate system. Upon the initial pop-up of the inductor, the parasitic capacitance due to the substrate drops, and therefore, the resonant frequency increases. As the 3D inductor becomes more compact at an increased compressive strain, the parasitic capacitance resulted from adjacent loops within the inductor increases, leading to a drop of the resonant frequency.

The vibrational performance of the 3D structures also changes evidently under increasing prestrain level. Figure 5b demonstrates two 3D structures with tunable resonant frequency, with the use of heterogeneous substrates similar to the one in Figure 5a to provide ultrahigh prestrains (350% and 400% in the left and right frames, respectively). These results display a monotonous decrease of fundamental resonant frequency as the prestrain increases. The eight-point star (Figure 5b, left) shows a tremendous drop (∼1.9 times in difference) of the fundamental resonant frequency from 19.0 GHz for the 2D shape to 10.2 GHz for the fully assembled 3D shape. The toroidal coils (Figure 5b, right) offer an even wider tunable range of fundamental resonant frequency from 1.8 to 4.9 GHz, corresponding to a 2.7 time difference.

3. CONCLUSIONS

This work presents a versatile approach to the design and fabrication of heterogeneous, deformable substrates to achieve mechanically guided assembly of spatially nonuniform 3D mesostructures. The heterogeneous substrates with tailored spatial variation of material modulus enable precise control over strain distributions, such as localized strain isolation and strain magnification upon uniform external stretching, which opens up more possibilities to achieve strain scaling for targeted device designs. Many delicate and sophisticated 3D structures, including those that resemble flowers, windmills, scorpions, and manta rays, have been deterministically assembled through the use of strategically designed heterogeneous, deformable substrates, with the aid of analytical and numerical modeling. The demonstrated characteristics of 3D structures are of application potential for microdevices like microelectromechanical systems and electromagnetic components, where the tunability and controllability of key performance indicators are essential.

4. EXPERIMENTAL METHODS

4.1. Fabrication of Heterogeneous Substrates by Casting and Curing. Fabrication of heterogeneous substrates by casting and curing started by forming the high-modulus components using 3D printing (Stratasys Objet Eden260VS 3D printer; VeroBlue RGD840 printing material, with an elastic modulus of ∼2 GPa). Fixing the printed high-modulus components onto a mold, followed by casting of an uncured precursor of a high-elongation elastomeric silicone (Dragon Skin 10 Slow) into the mold to fill cavities and curing in a vacuum chamber at room temperature for ∼6 h, forms the heterogeneous substrate. Gently releasing the substrate from the mold completes the fabrication process. Figure S22a (Supporting Information) shows the experimental procedures of casting and curing heterogeneous substrates.

4.2. Fabrication of Heterogeneous Substrates by 3D Printing. Fabrication of heterogeneous substrates by 3D printing started by uploading generated computer-aided design (CAD) models incorporating parts of different moduli onto a 3D printer (Stratasys Objet350 Connex3 printer) that is capable of printing seven available rubber-like materials within a single sample. The mechanical properties of the seven rubber-like printing materials have been measured through tensile testing and are presented in Figure S23 (Supporting Information). Additional procedures such as removing the supporting materials underneath the heterogeneous substrate are also necessary to complete the process (Figure S22b, Supporting Information).

4.3. Fabrication of 3D Mesostructures. Fabrication of 3D mesostructures started by mechanical or laser cutting thin films/foils made of various materials (copper, PET, polyimide, etc.) into desired 2D geometries. Retrieving thin films/foils from their adhesive supporting mat after cutting was completed with the aid of water-soluble tapes. Applying an adhesive (Gorilla Super Glue) at the locations for bonding sites, transferring the 2D precursor structures onto the prestretched heterogeneous substrate, and curing for ∼5 min at room temperature induced strong interfacial adhesion at the bonding sites. Gradually releasing the prestretched heterogeneous substrate concluded the assembly of 3D mesostructures. Figure S24 (Supporting Information) shows the experimental procedures of popping up 3D structures on heterogeneous substrates.

4.4. Experimental Visualization of Strain Fields of Heterogeneous Substrates. Experimental visualization of strain fields of heterogeneous substrates started by forming an array of copper dots (for uniaxially stretched substrates, thickness 100 nm, diameter of each dot 600 μm, and spacing 1500 μm; for biaxially/multiaxially stretched substrates, thickness 100 nm, diameter of each dot 450 μm, and spacing 1000 μm) by ion beam sputtering, with the aid of a shadow mask, on the surface of an undeformed substrate. These metal dots served as displacement markers. A single-lens reflex (SLR) camera collected a series of optical images of the heterogeneous substrates during stretching (Figure S25, Supporting Information). Images were processed in MATLAB (version 2017b) for automated positioning of the dots. The strain components at each dot were then calculated based on the relative displacements of adjacent dots with the central differencing scheme.

■ ASSOCIATED CONTENT

Ⓢ Supporting Information

The Supporting Information is available free of charge on the ACS Publications website at DOI: 10.1021/acsami.8b19187.

> Pros and cons of fabricating heterogeneous substrates using 3D printing approach versus casting and curing approach, finite element analysis, analytical model for heterogeneous substrates with unidirectional variation (continuous or abrupt) of modulus under uniaxial stretching, and electromagnetic simulations (PDF)

AUTHOR INFORMATION

Corresponding Author

*E-mail: yihuizhang@tsinghua.edu.cn.

ORCID

Haiwen Luan: 0000-0003-0722-1108
Xu Cheng: 0000-0001-7536-945X
Yihui Zhang: 0000-0003-0885-2067

Present Address

[#]Department of Mechanical Engineering, Northwestern University, Evanston, Illinois 60208, USA.

Author Contributions

H.L. and X.C. contributed equally to this work. H.L., X.C., Y.H., and Y.Z. conceived the idea and designed the research; H.L. and X.C. led the mechanical modeling and theoretical studies, with assistance from A.W., S.Z., H.W., Z.X., K.L., and Y.X; X.C. and A.W. performed the fabrication of heterogeneous substrates and 3D structures, with assistance from K.B., W.P., and F.Z; H.L. and X.C. performed the strain visualization studies of heterogeneous substrates, with assistance from S.Z. and H.W; H.L., X.C., and Y.Z. wrote the manuscript and designed the figures. All authors commented on the manuscript and have given approval to the final version of the manuscript.

Notes

The authors declare no competing financial interest.

ACKNOWLEDGMENTS

Y.Z. acknowledges the support from the National Natural Science Foundation of China (grant nos. 11502129 and 11722217) and the Tsinghua National Laboratory for Information Science and Technology. Y.H. acknowledges the support from the NSF (grant nos. CMMI1400169, CMMI1534120 and CMMI1635443). H.L. acknowledged the support from the Martin Fellowship of Northwestern University. Y.X. acknowledged the support from the Ryan Fellowship and the Northwestern University International Institute for Nanotechnology.

ABBREVIATIONS

3D, three-dimensional
2D, two-dimensional
UV, ultraviolet
FEA, finite element analysis
PI, polyimide
PET, polyethylene terephthalate
CAD, computer-aided design
SLR, single lens reflex
NSF, National Science Foundation

REFERENCES

(1) Felton, S.; Tolley, M.; Demaine, E.; Rus, D.; Wood, R. A Method for Building Self-Folding Machines. *Science* **2014**, *345*, 644–646.

(2) Yu, C.; Gao, H.; Yu, H.; Jiang, H.; Cheng, G. J. Laser Dynamic Forming of Functional Materials Laminated Composites on Patterned Three-Dimensional Surfaces with Applications on Flexible Microelectromechanical Systems. *Appl. Phys. Lett.* **2009**, *95*, 091108.

(3) Huang, G.; Mei, Y. Assembly and Self-Assembly of Nanomembrane Materials—from 2D to 3D. *Small* **2018**, *14*, 1703665.

(4) Huang, W.; Zhou, J.; Froeter, P. J.; Walsh, K.; Liu, S.; Kraman, M. D.; Li, M.; Michaels, J. A.; Sievers, D. J.; Gong, S.; Li, X. Three-Dimensional Radio-Frequency Transformers Based on a Self-Rolled-up Membrane Platform. *Nat. Electron.* **2018**, *1*, 305–313.

(5) Yu, X.; Huang, W.; Li, M.; Comberiate, T. M.; Gong, S.; Schutt-Aine, J. E.; Li, X. Ultra-Small, High-Frequency, and Substrate-Immune Microtube Inductors Transformed from 2D to 3D. *Sci. Rep.* **2015**, *5*, 9661.

(6) Yu, C.; Duan, Z.; Yuan, P.; Li, Y.; Su, Y.; Zhang, X.; Pan, Y.; Dai, L. L.; Nuzzo, R. G.; Huang, Y.; Jiang, H.; Rogers, J. A. Electronically Programmable, Reversible Shape Change in Two- and Three-Dimensional Hydrogel Structures. *Adv. Mater.* **2013**, *25*, 1541–1546.

(7) Zhao, Y.; Huang, G.; Li, Y.; Edy, R.; Gao, P.; Tang, H.; Bao, Z.; Mei, Y. Three-Dimensional Carbon/ZnO Nanomembrane Foam as an Anode for Lithium-Ion Battery with Long-Life and High Areal Capacity. *J. Mater. Chem. A* **2018**, *6*, 7227–7235.

(8) Arpin, K. A.; Mihi, A.; Johnson, H. T.; Baca, A. J.; Rogers, J. A.; Lewis, J. A.; Braun, P. V. Multidimensional Architectures for Functional Optical Devices. *Adv. Mater.* **2010**, *22*, 1084–1101.

(9) Li, J.; Liang, G.; Zhu, X.; Yang, S. Exploiting Nanoroughness on Holographically Patterned Three-Dimensional Photonic Crystals. *Adv. Funct. Mater.* **2012**, *22*, 2980–2986.

(10) Soukoulis, C. M.; Wegener, M. Past Achievements and Future Challenges in the Development of Three-Dimensional Photonic Metamaterials. *Nat. Photonics* **2011**, *5*, 523–530.

(11) Grimm, D.; Bof Bufon, C. C.; Deneke, C.; Atkinson, P.; Thurmer, D. J.; Schäffel, F.; Gorantla, S.; Bachmatiuk, A.; Schmidt, O. G. Rolled-up Nanomembranes as Compact 3D Architectures for Field Effect Transistors and Fluidic Sensing Applications. *Nano Lett.* **2012**, *13*, 213–218.

(12) Liu, Y.; Pharr, M.; Salvatore, G. A. Lab-on-Skin: A Review of Flexible and Stretchable Electronics for Wearable Health Monitoring. *ACS Nano* **2017**, *11*, 9614–9635.

(13) Yang, Y.; Gao, W. Wearable and Flexible Electronics for Continuous Molecular Monitoring. *Chem. Soc. Rev.* **2018**, DOI: 10.1039/C7CS00730B.

(14) Li, X.; Gao, H. Mechanical Metamaterials: Smaller and Stronger. *Nat. Mater.* **2016**, *15*, 373–374.

(15) Overvelde, J. T. B.; de Jong, T. A.; Shevchenko, Y.; Becerra, S. A.; Whitesides, G. M.; Weaver, J. C.; Hoberman, C.; Bertoldi, K. A Three-Dimensional Actuated Origami-Inspired Transformable Metamaterial with Multiple Degrees of Freedom. *Nat. Commun.* **2016**, *7*, 10929.

(16) Overvelde, J. T. B.; Weaver, J. C.; Hoberman, C.; Bertoldi, K. Rational Design of Reconfigurable Prismatic Architected Materials. *Nature* **2017**, *541*, 347–352.

(17) Shan, S.; Kang, S. H.; Raney, J. R.; Wang, P.; Fang, L.; Candido, F.; Lewis, J. A.; Bertoldi, K. Multistable Architected Materials for Trapping Elastic Strain Energy. *Adv. Mater.* **2015**, *27*, 4296–4301.

(18) Silverberg, J. L.; Evans, A. A.; McLeod, L.; Hayward, R. C.; Hull, T.; Santangelo, C. D.; Cohen, I. Using Origami Design Principles to Fold Reprogrammable Mechanical Metamaterials. *Science* **2014**, *345*, 647–650.

(19) Eidini, M.; Paulino, G. H. Unraveling Metamaterial Properties in Zigzag-Base Folded Sheets. *Sci. Adv.* **2015**, *1*, No. e1500224.

(20) Filipov, E. T.; Tachi, T.; Paulino, G. H. Origami Tubes Assembled into Stiff, yet Reconfigurable Structures and Metamaterials. *Proc. Natl. Acad. Sci. U.S.A.* **2015**, *112*, 12321–12326.

(21) Tang, Y.; Lin, G.; Yang, S.; Yi, Y. K.; Kamien, R. D.; Yin, J. Programmable Kiri-Kirigami Metamaterials. *Adv. Mater.* **2017**, *29*, 1604262.

(22) Pan, L.; Yu, G.; Zhai, D.; Lee, H. R.; Zhao, W.; Liu, N.; Wang, H.; Tee, B. C.-K.; Shi, Y.; Cui, Y.; Bao, Z. Hierarchical Nanostructured Conducting Polymer Hydrogel with High Electrochemical Activity. *Proc. Natl. Acad. Sci. U.S.A.* **2012**, *109*, 9287–9292.

(23) Pikul, J. H.; Zhang, H. G.; Cho, J.; Braun, P. V.; King, W. P. High-Power Lithium Ion Microbatteries from Interdigitated Three-Dimensional Bicontinuous Nanoporous Electrodes. *Nat. Commun.* **2013**, *4*, 1732.

(24) Sun, K.; Wei, T.-S.; Ahn, B. Y.; Seo, J. Y.; Dillon, S. J.; Lewis, J. A. 3D Printing of Interdigitated Li-Ion Microbattery Architectures. *Adv. Mater.* **2013**, *25*, 4539−4543.

(25) Zhang, H.; Yu, X.; Braun, P. V. Three-Dimensional Bicontinuous Ultrafast-Charge and -Discharge Bulk Battery Electrodes. *Nat. Nanotechnol.* **2011**, *6*, 277−281.

(26) Eckel, Z. C.; Zhou, C.; Martin, J. H.; Jacobsen, A. J.; Carter, W. B.; Schaedler, T. A. Additive Manufacturing of Polymer-Derived Ceramics. *Science* **2016**, *351*, 58−62.

(27) Gladman, A. S.; Matsumoto, E. A.; Nuzzo, R. G.; Mahadevan, L.; Lewis, J. A. Biomimetic 4D printing. *Nat. Mater.* **2016**, *15*, 413−418.

(28) Skylar-Scott, M. A.; Gunasekaran, S.; Lewis, J. A. Laser-Assisted Direct Ink Writing of Planar and 3D Metal Architectures. *Proc. Natl. Acad. Sci. U.S.A.* **2016**, *113*, 6137−6142.

(29) Truby, R. L.; Lewis, J. A. Printing Soft Matter in Three Dimensions. *Nature* **2016**, *540*, 371−378.

(30) Su, J.-W.; Tao, X.; Deng, H.; Zhang, C.; Jiang, S.; Lin, Y.; Lin, J. 4D Printing of a Self-Morphing Polymer Driven by a Swellable Guest Medium. *Soft Matter* **2018**, *14*, 765−772.

(31) Zhang, Y.; Zhang, F.; Yan, Z.; Ma, Q.; Li, X.; Huang, Y.; Rogers, J. A. Printing, Folding and Assembly Methods for Forming 3D Mesostructures in Advanced Materials. *Nat. Rev. Mater.* **2017**, *2*, 17019.

(32) Cumpston, B. H.; Ananthavel, S. P.; Barlow, S.; Dyer, D. L.; Ehrlich, J. E.; Erskine, L. L.; Heikal, A. A.; Kuebler, S. M.; Lee, I.-Y. S.; McCord-Maughon, D.; Qin, J.; Röckel, H.; Rumi, M.; Wu, X.-L.; Marder, S. R.; Perry, J. W. Two-Photon Polymerization Initiators for Three-Dimensional Optical Data Storage and Microfabrication. *Nature* **1999**, *398*, 51−54.

(33) Jang, D.; Meza, L. R.; Greer, F.; Greer, J. R. Fabrication and Deformation of Three-Dimensional Hollow Ceramic Nanostructures. *Nat. Mater.* **2013**, *12*, 893−898.

(34) LaFratta, C. N.; Fourkas, J. T.; Baldacchini, T.; Farrer, R. A. Multiphoton Fabrication. *Angew. Chem., Int. Ed.* **2007**, *46*, 6238−6258.

(35) Schmidt, O. G.; Eberl, K. Thin Solid Films Roll up into Nanotubes. *Nature* **2001**, *410*, 168.

(36) Wei, Z.; Jia, Z.; Athas, J.; Wang, C.; Raghavan, S. R.; Li, T.; Nie, Z. Hybrid Hydrogel Sheets That Undergo Pre-Programmed Shape Transformations. *Soft Matter* **2014**, *10*, 8157−8162.

(37) Wang, H.; Liang, Y.; Gao, W.; Dong, R.; Wang, C. Emulsion Hydrogel Soft Motor Actuated by Thermal Stimulation. *ACS Appl. Mater. Interfaces* **2017**, *9*, 43211−43219.

(38) Sprinkle, M.; Ruan, M.; Hu, Y.; Hankinson, J.; Rubio-Roy, M.; Zhang, B.; Wu, X.; Berger, C.; de Heer, W. A. Scalable Templated Growth of Graphene Nanoribbons on SiC. *Nat. Nanotechnol.* **2010**, *5*, 727−731.

(39) Jin, B.; Song, H.; Jiang, R.; Song, J.; Zhao, Q.; Xie, T. Programming a Crystalline Shape Memory Polymer Network with Thermo- and Photo-Reversible Bonds toward a Single-Component Soft Robot. *Sci. Adv.* **2018**, *4*, No. eaao3865.

(40) Zhang, C.; Su, J.-W.; Deng, H.; Xie, Y.; Yan, Z.; Lin, J. Reversible Self-Assembly of 3D Architectures Actuated by Responsive Polymers. *ACS Appl. Mater. Interfaces* **2017**, *9*, 41505−41511.

(41) Huang, L.; Jiang, R.; Wu, J.; Song, J.; Bai, H.; Li, B.; Zhao, Q.; Xie, T. Ultrafast Digital Printing toward 4D Shape Changing Materials. *Adv. Mater.* **2017**, *29*, 1605390.

(42) Xu, W.; Qin, Z.; Chen, C.-T.; Kwag, H. R.; Ma, Q.; Sarkar, A.; Buehler, M. J.; Gracias, D. H. Ultrathin Thermoresponsive Self-Folding 3D Graphene. *Sci. Adv.* **2017**, *3*, No. e1701084.

(43) Kobayashi, K.; Oh, S. H.; Yoon, C.; Gracias, D. H. Multitemperature Responsive Self-Folding Soft Biomimetic Structures. *Macromol. Rapid Commun.* **2018**, *39*, 1700692.

(44) Xu, S.; Yan, Z.; Jang, K.-I.; Huang, W.; Fu, H.; Kim, J.; Wei, Z.; Flavin, M.; McCracken, J.; Wang, R.; Badea, A.; Liu, Y.; Xiao, D.; Zhou, G.; Lee, J.; Chung, H. U.; Cheng, H.; Ren, W.; Banks, A.; Li, X.; Paik, U.; Nuzzo, R. G.; Huang, Y.; Zhang, Y.; Rogers, J. A. Assembly of Micro/Nanomaterials into Complex, Three-Dimensional Architectures by Compressive Buckling. *Science* **2015**, *347*, 154−159.

(45) Yan, Z.; Zhang, F.; Liu, F.; Han, M.; Ou, D.; Liu, Y.; Lin, Q.; Guo, X.; Fu, H.; Xie, Z.; Gao, M.; Huang, Y.; Kim, J.; Qiu, Y.; Nan, K.; Kim, J.; Gutruf, P.; Luo, H.; Zhao, A.; Hwang, K.-C.; Huang, Y.; Zhang, Y.; Rogers, J. A. Mechanical Assembly of Complex, 3D Mesostructures from Releasable Multilayers of Advanced Materials. *Sci. Adv.* **2016**, *2*, No. e1601014.

(46) Yan, Z.; Zhang, F.; Wang, J.; Liu, F.; Guo, X.; Nan, K.; Lin, Q.; Gao, M.; Xiao, D.; Shi, Y.; Qiu, Y.; Luan, H.; Kim, J. H.; Wang, Y.; Luo, H.; Han, M.; Huang, Y.; Zhang, Y.; Rogers, J. A. Controlled Mechanical Buckling for Origami-Inspired Construction of 3D Microstructures in Advanced Materials. *Adv. Funct. Mater.* **2016**, *26*, 2629−2639.

(47) Zhang, Y.; Yan, Z.; Nan, K.; Xiao, D.; Liu, Y.; Luan, H.; Fu, H.; Wang, X.; Yang, Q.; Wang, J.; Ren, W.; Si, H.; Liu, F.; Yang, L.; Li, H.; Wang, J.; Guo, X.; Luo, H.; Wang, L.; Huang, Y.; Rogers, J. A. A Mechanically Driven Form of Kirigami as a Route to 3D Mesostructures in Micro/Nanomembranes. *Proc. Natl. Acad. Sci. U.S.A.* **2015**, *112*, 11757−11764.

(48) Fu, H.; Nan, K.; Bai, W.; Huang, W.; Bai, K.; Lu, L.; Zhou, C.; Liu, Y.; Liu, F.; Wang, J.; Han, M.; Yan, Z.; Luan, H.; Zhang, Y.; Zhang, Y.; Zhao, J.; Cheng, X.; Li, M.; Lee, J. W.; Liu, Y.; Fang, D.; Li, X.; Huang, Y.; Zhang, Y.; Rogers, J. A. Morphable 3D Mesostructures and Microelectronic Devices by Multistable Buckling Mechanics. *Nat. Mater.* **2018**, *17*, 268−276.

(49) Humood, M.; Shi, Y.; Han, M.; Lefebvre, J.; Yan, Z.; Pharr, M.; Zhang, Y.; Huang, Y.; Rogers, J. A.; Polycarpou, A. A. Fabrication and Deformation of 3D Multilayered Kirigami Microstructures. *Small* **2018**, *14*, 1703852.

(50) Fu, H.; Nan, K.; Froeter, P.; Huang, W.; Liu, Y.; Wang, Y.; Wang, J.; Yan, Z.; Luan, H.; Guo, X.; Zhang, Y.; Jiang, C.; Li, L.; Dunn, A. C.; Li, X.; Huang, Y.; Zhang, Y.; Rogers, J. A. Mechanically-Guided Deterministic Assembly of 3D Mesostructures Assisted by Residual Stresses. *Small* **2017**, *13*, 1700151.

(51) Fan, Z.; Hwang, K.-C.; Rogers, J. A.; Huang, Y.; Zhang, Y. A Double Perturbation Method of Postbuckling Analysis in 2D Curved Beams for Assembly of 3D Ribbon-Shaped Structures. *J. Mech. Phys. Solids* **2018**, *111*, 215−238.

(52) Zhang, Q.; Yin, J. Spontaneous Buckling-Driven Periodic Delamination of Thin Films on Soft Substrates under Large Compression. *J. Mech. Phys. Solids* **2018**, *118*, 40−57.

(53) Nan, K.; Luan, H.; Yan, Z.; Ning, X.; Wang, Y.; Wang, A.; Wang, J.; Han, M.; Chang, M.; Li, K.; Zhang, Y.; Huang, W.; Xue, Y.; Huang, Y.; Zhang, Y.; Rogers, J. A. Engineered Elastomer Substrates for Guided Assembly of Complex 3D Mesostructures by Spatially Nonuniform Compressive Buckling. *Adv. Funct. Mater.* **2017**, *27*, 1604281.

(54) Cotton, D. P. J.; Popel, A.; Graz, I. M.; Lacour, S. P. Photopatterning the Mechanical Properties of Polydimethylsiloxane Films. *J. Appl. Phys.* **2011**, *109*, 054905.

(55) Sun, Y.; Jiang, L.-T.; Okada, R.; Fu, J. UV-Modulated Substrate Rigidity for Multiscale Study of Mechanoresponsive Cellular Behaviors. *Langmuir* **2012**, *28*, 10789−10796.

(56) Li, T.; Wang, J.; Zhang, L.; Yang, J.; Yang, M.; Zhu, D.; Zhou, X.; Handschuh-Wang, S.; Liu, Y.; Zhou, X. "Freezing", Morphing, and Folding of Stretchy Tough Hydrogels. *J. Mater. Chem. B* **2017**, *5*, 5726−5732.

(57) Libanori, R.; Erb, R. M.; Reiser, A.; Le Ferrand, H.; Süess, M. J.; Spolenak, R.; Studart, A. R. Stretchable Heterogeneous Composites with Extreme Mechanical Gradients. *Nat. Commun.* **2012**, *3*, 1265.